20th International Conference on Ground Control in Mining

NUMERICAL SIMULATION ON MICROSEISMICITY DUE TO MINING AT ONE OF THE COLLIERIES IN AUSTRALIA

Fujii, Y., Associate Professor, Hokkaido University, Sapporo, Hokkaido, Japan
Balusu, R., Senior Mining Engineer, CSIRO Exploration and Mining, Brisbane, QLD, Australia
Deguchi, G., Manager, JCOAL, Chiyoda-ku, Tokyo, Japan
Ishijima, Y., Professor, Hokkaido University, Sapporo, Hokkaido, Japan

ABSTRACT

Numerical simulation for microseismicity due to mining at one of the collieries in Australia was carried out and the results were compared to the observed microseismicity.

3-D Stress analysis showed stress concentration on the edges of the mined areas and on the coal pillars. The stress concentration ahead of the coal face was biased to the tailgate. This is similar to the observed distribution of microseismic events. Stress reduction above and below the mined area was seen. Tensile stress was observed mainly above the mined area. It was realized that compressive failure due to nearly vertical maximum principal stress and nearly horizontal minimum principal stress in retreat direction (NS) might occur ahead of the face. Tensile failure due to nearly vertical minimum principal stress above the mined area was expected. Compressive failure due to nearly horizontal maximum principal stress in EW direction and nearly vertical minimum principal stress above and below the mined area were also expected.

Numerical simulation based on Seismic Moment Method was carried out first with a standard initial stress and strength data set. Broken elements were mainly distributed 0 to 100 m ahead of the face with more such elements in the roof than in the floor. Distribution of the broken elements with relatively small maximum shear seismic moments in plan view was biased to the tailgate. On the other hand, broken elements with relatively large maximum shear seismic moments distributed evenly. This behavior is similar to the observation that weak microseismic events showed a biased distribution while the strong ones were distributed evenly. The height of the yield zone was initially 30 m. It increased gradually up to 200 m until the face reached 500 m from the setup entry and then it was kept almost constant. These features are comparable to the microseismic observation.

Effects of strength on the simulated results were then investigated. It was confirmed that the larger the strength data, the smaller the yield zone. Similar features to microseismic observation were obtained for the results with smaller strength data although there was no similarity between the simulated results with larger strength data and the microseismic observation. The selected best strength data values were much smaller than the laboratory values.

Effects of initial horizontal stress were then investigated. The biased distribution of broken elements was not observed when smaller horizontal stresses were assumed. Broken elements appeared behind the face when larger horizontal stresses in the retreat direction were used.

Finally, effects of panel layout were investigated by carrying out simulation for three imaginary panel layouts. Stress concentration on the edges of mined area was significantly small when there were no gobs around the panel of interest. Neither the biased distribution of the stress concentration nor that of broken elements was seen. No significant difference in the height of the yield zone and its growth behavior from the standard case was observed. In the case where the setup entry was set parallel to that of LW3, results were almost the same as the standard case. In the case where the setup entry position was 210 m ahead of that of LW3, biased stress concentration area behind the setup entry was observed. Broken elements concentration on the setup entry was observed in an initial stage of mining.

INTRODUCTION

Gas drainage is one of the problems that should be solved at one of the collieries in Australia. The project group of Mining and Exploration, CSIRO carried out microseismic monitoring for LW4 at the mine in order to obtain information for effective gas drainage. It will be useful if microseismicity can be numerically predicted because a prediction provides suggestions about microseismic monitoring and gas drainage operations. Moreover, comparison between prediction and monitoring results will be useful to understand deformation and failure mechanism of rock mass around longwall mining panels.

Many attempts have been made to predict rockbursts at coal faces as well as microseismicity in underground mines. For instance, Cook et al. [1] found a correlation between rockburst occurrence and calculated energy release rate. Sugawara et al. [2] compared microseismic intensity to the calculated energy release rate. However, no prediction on location could be given since failure could not be considered in the analyses by energy release rate. The excess shear stress concept was developed by South African researchers (McGarr & Wiebols [3], Ryder, [4], Spottiswoode, [5, 6]). This index also could not indicate the location and intensity of microseismic events or rockbursts.

Areas where microseismic events concentrate and the variation of microseismic intensity with respect to face advance were successfully predicted by the strain energy release rate method proposed by Fujii and Ishijima [7]. The value of their computed seismic energy release rate was, however, ten thousand times the observed one. In 1991, Fujii and Ishijima [8] proposed a new method. The predicted and monitored maximum shear seismic moment release rates were now having the same magnitude and showing the same behavior. In the above method, only failure of the rock mass was considered and that in coal seam was ignored. Therefore, a further modification was done by Fujii et al. [9] and the modified method was proposed as Seismic Moment Method. Case studies in Horonai Coal Mine and in Miike Coal Mine, Japan were described in the paper. Rockbursts that occurred at both mines as well as microseismicity were successfully predicted in the case studies.

This paper will first outline Seismic Moment Method with a slight modification in the evaluation of the maximum shear seismic moment. Then the results of 3-D elastic stress analysis on LW4 by using Displacement

Discontinuity Method [10] will be shown. Normal stress distribution will be compared to the distribution of the observed microseismic events. Detailed stress distribution around the face will also be shown considering possible failure mode. Next, the results of numerical simulation on microseismicity by using Seismic Moment Method will be shown. Occurrence of elements' failure and its variation with face advance will be displayed. The distribution of broken elements will be compared to that of the observed microseismic events. Effects of strength and initial stress data on simulated results will then be investigated. Finally, simulation for several imaginary panel layouts will be carried out in order to investigate effects of panel layout on failure around longwall mining panels.

SEISMIC MOMENT METHOD

Definition of maximum shear seismic moment

The seismic moment tensor, M_{pq}, is a fundamental physical quantity in seismology and is related to the displacement in the rock mass, u_n, in x_n-direction by the following equations for a fault source [11].

$$u_n = \int \left(\frac{dM_{pq}}{dA} * \frac{\partial G_{np}}{\partial x_q} \right) dA \tag{1}$$

where
* : convolution symbol;
G_{np} : Green function;
A : fault area.

M_{pq} is represented by the following equations,

$$M_{pq} = \int [u_i] n_j c_{ijpq} dA \tag{2}$$

where,
c_{ijpq} : elastic constants;
$[u_i]$: displacement discontinuity;
n_j : unit normal vector of the fault.

The maximum shear seismic moment, M_s, is a scalar quantity, defined for each microseismic event as follows:

$$M_s = \frac{M_1 - M_3}{2} \tag{3}$$

where M_1 and M_3 are the maximum and minimum principal values of the seismic moment tensor. The maximum shear seismic moment represents a magnitude of the seismic moment tensor. It becomes equivalent to the seismic moment, M, a scalar quantity which is used in seismology if the focal mechanism is of the double-couple model.

Numerical procedure

The brief outline of Seismic Moment Method is described (Fig. 1). The 3-D elastic stress analysis by using Displacement Discontinuity Method is progressively carried out first for each mining step of 30 m in order to make a data file on displacement discontinuity of each element. And then software for simulation is run to evaluate element breakage and maximum shear seismic moment.

Strictly speaking, a 3-D elasto-plastic code is required for Seismic Moment Method. The reasons why the authors used an elastic code are as follows; (1) the authors do not have access to a 3-D elasto-plastic code; and (2) the authors do not think that 3-D elasto-plastic analyses for longwall mining have already become a practical means. Actually, CPU time just for the elastic analysis described later was about 4 hours by a super computer. It would take at least ten times the CPU time if an elasto-plastic analysis is carried out. The following assumptions were required using an elastic analysis code; (1) the stress state is determined using an elastic analysis; and, (2) any element whose stress state is satisfied by a given failure criterion is regarded as broken. The error due to these assumptions increases with the value of stress drop [7]. An evaluation procedure for the stress state in the coal seam, which is required in order to consider coal seam failure, is given in Appendix.

The simulation procedure is as follows (Fig. 2).

(1) The coal seam is divided into square elements (coal seam elements) having the side lengths of $2h$ (30 m); while the rock mass above and below the coal seam is divided into cubic elements (rock mass elements) having side lengths of $2h$. The thickness of the region of interest was set at ±270 m from the coal seam.
(2) A failure parameter of 0 is assigned to both the coal seam elements and rock mass elements as initial values and the stress state at the center of each element is calculated for the case where only mined panels exist. The stress states are then compared to a tensile failure criterion. The failure parameter is changed to 1 if the tensile failure criterion is satisfied. If the element remains intact, the stress state is then compared to Coulomb's criterion. The failure parameter is changed to 2 if the criterion is satisfied.
(3) The stress state at the center of elements whose failure parameter is 0 is calculated for the case where the coal face advances by $2h$ (30 m) and is compared to the failure criteria. The maximum shear seismic moment is calculated and the failure parameter is changed if an element breaks.
(4) The third step is iterated until the mining sequence is terminated.

Maximum shear seismic moment due to failure of element

This quantity was evaluated considering stiffness of the surrounding medium in the previous paper [9]. This was because the broken element was located only ahead of the face and it was easy to classify their boundary conditions according to their location. However, failure of rock elements above and below the mined area was also anticipated for Mine A case and the boundary condition for each broken element varies significantly depending upon the location of the element. It would be difficult to estimate precisely the stiffness of the surrounding medium for Mine A case. The following method was therefore used instead of the published method. Namely, it was assumed that a circular rupture plane, with radius h and center located at the center of the element, appeared when a failure criterion of the element was satisfied.

The method for a tensile failure of a rock element is described first. Miyamoto [12] shows displacement discontinuity due to normal stress $\Delta\sigma$ at distance r from the center of a penny-shaped crack, which is perpendicular to z-axis and has radius h, as the following equation.

$$[u_z] = \frac{8\Delta\sigma(1-\nu^2)}{\pi E}\sqrt{h^2 - r^2} \tag{4}$$

where ν is Poisson's ratio. Average displacement discontinuity can be evaluated as follows.

$$[\overline{u}_z] = \frac{\int [u_z] dA}{A} = \frac{16\Delta\sigma(1-\nu^2)h}{3\pi E} \tag{5}$$

For a sufficiently small fault source, Eq. (2) can be rewritten as the following equation.

$$M_{pq} = [u_i] n_j c_{ijpq} A \tag{6}$$

Non-zero components of seismic moment tensor are therefore as follows;

$$M_{xx} = M_{yy} = \frac{16\Delta\sigma(1-\nu)\nu h^3}{3(1-2\nu)} \tag{7}$$

$$M_{zz} = \frac{16\Delta\sigma(1-\nu)^2 h^3}{3(1-2\nu)}. \tag{8}$$

Substituting Eqs. (7) and (8) into Eq. (3), we get,

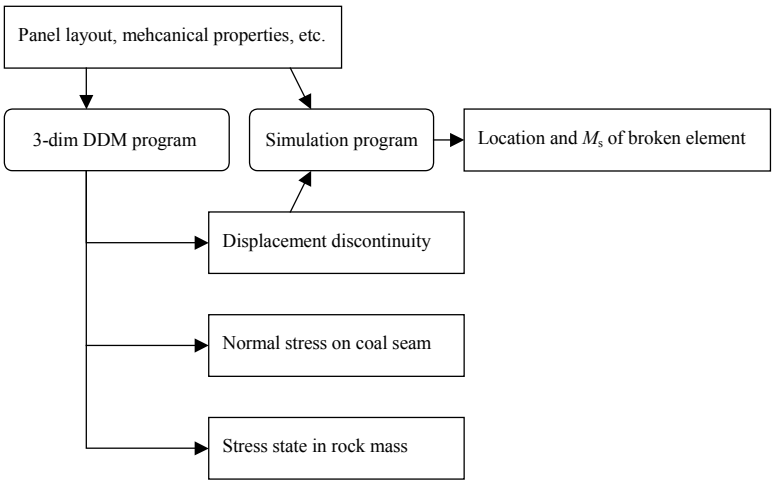

Fig. 1 Procedure of Seismic Moment Method

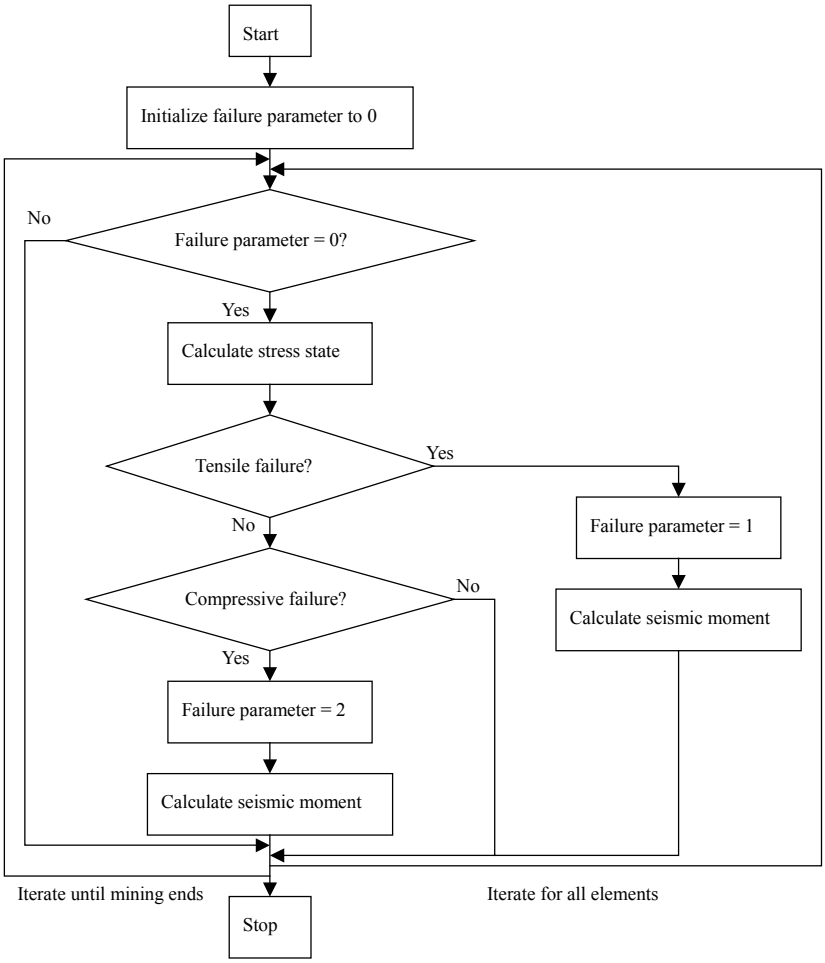

Fig. 2 Flow chart of the simulation program

$$M_s = \frac{8\Delta\sigma(1-\nu)h^3}{3} \quad (9)$$

Assuming that a sheet like inclusion rock in the crack fails in a tensile manner and the stress drop is $\Delta\sigma$, Eq. (9) can be used to evaluate maximum shear seismic moment due to tensile failure of a rock element containing the crack.

The method for a compressive failure of a rock element is given below. Sato & Kinoshita [13] showed displacement discontinuity due to shear stress $\Delta\tau$ at distance r from the center of a penny-shaped crack, which is perpendicular to z-axis and has radius h, as the following equation.

$$[u_x] = \frac{8\Delta\tau(1-\nu)}{\pi(2-\nu)G}\left(h - \frac{r^2}{h+\sqrt{h^2-r^2}}\right) \quad (10)$$

Average displacement discontinuity can be evaluated as follows.

$$[\bar{u}_x] = \frac{32\Delta\tau(1-\nu^2)h}{3\pi(2-\nu)E} \quad (11)$$

Non-zero components of seismic moment tensor and the maximum shear seismic moment can be evaluated in the similar way to the tensile failure case.

$$M_{xz} = M_{zx} = M_s = \frac{16\Delta\tau(1-\nu)h^3}{3(2-\nu)} \quad (12)$$

Assuming that a sheet like inclusion rock in the crack fails in a shear manner and the stress drop is $\Delta\tau$, Eq. (12) can be used to evaluate maximum shear seismic moment due to shear failure of a rock element containing the crack. Basically, Eqs. (9) and (12) can also be used for the failure of a coal seam element.

ELASTIC STRESS ANALYSIS

The mining area was divided into 40 x 85 elements (Fig. 3). The size of each element is 30 x 30 m. It was assumed that the shallower edge of the mining area is located at 200 m below the ground surface and the average dip is 5°. Rock masses above and below the coal seam were assumed to be homogenous. The mechanical properties shown in Table 1 were used in the simulation.

The calculation took about 30 min by a Pentium II 450 MHz PC. Fig. 4 shows an example of the normal stress distribution on the coal seam. Stress concentration can be seen on the edges of the mined panels. The highest stress concentration can be seen on the coal pillars between LW2 and LW3. There appears rather wide area of stress concentration ahead of the face of LW4. The normal stress is higher near the tailgate than the maingate. In the microseismic observation, most events locate between the coal face and 100 m ahead of it (Fig. 5a). The center of the distribution is biased to the tailgate. This feature is similar to the calculated stress concentration.

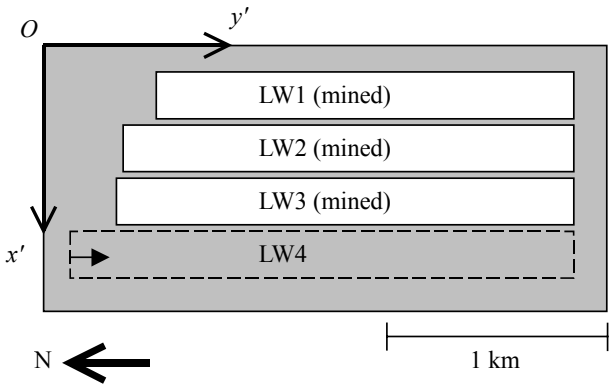

Fig. 3 Panel layout

Table 1 Parameters used in the elastic analysis

E_{rock} / E_{coal}	2
Poisson' ratio	0.2
Vertical stress	Product of specific gravity and depth
Specific gravity	27 kN/m^3
σ_x (EW)	1.20 σ_V
σ_y (NS)	0.48 σ_V
Working height	4.5 m

Fig. 4 An example of normal stress distribution on the coal seam. The gray scale between black to white denotes the normal stress of 0 to 40 MPa.

Let's investigate the stress distribution in detail. Fig. 6 shows stress distribution along y''-axis (O'' is taken at the center of the coal face) at 1020 m face advance. The vertical stress concentration at the coal face can be seen. Rock elements near the coal seam and/or coal seam elements would break ahead of the face if the compressive strength is small. The vertical stress decreases above and below the mined area. The vertical stress in the floor remains as compressive (Fig. 6b). On the other hand, some of the vertical stress data in the roof are tensile (Fig. 6a) because of the effects of the gravity force. Tensile failure due to vertical tensile stress might occur above the mined area if tensile strength of rock element is small. Compressive failure may occur due to the maximum principal stress in EW direction and the nearly vertical minimum principal stress even if the tensile failure does not occur.

NUMERICAL SIMULATION

Panel layout is already shown in Fig. 3. Numerical simulation was carried out for several cases. Each case is specified as Case X-n(-x) where X, n and x denote initial stress variation (Table 2), strength variation (Table3) and variation in panel layout, respectively. The results for Case A-1, which will be referred later as a standard case, are shown in this chapter.

Simulation took about four hours by a super computer (Hitachi SR8000, 320 GB memory, 32 nodes, 1.1 TB HD, 256 GFLOPS) at Hokkaido University Computing Center, Japan. Broken elements are shown in Fig. 7.

In the initial stage of mining, the broken elements locate in the vicinity of the face. The broken rock elements that locate at the edges of mined area are due to the nearly vertical maximum principal stress and the minimum principal stress nearly in the retreat direction. On the other hand, the broken

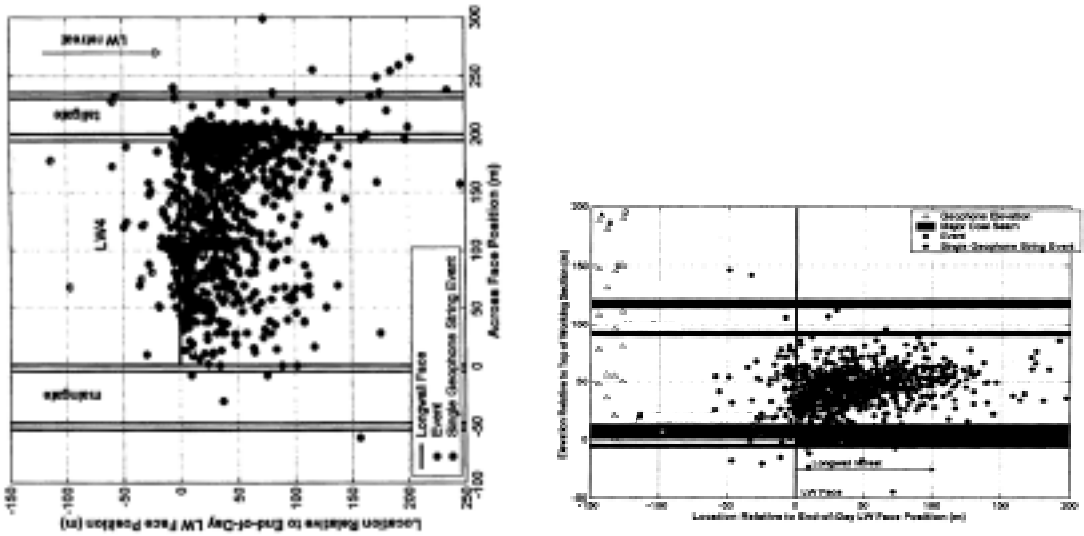

(a) Plan view (b) Sectional view

Fig. 5 Observed distribution of microseismic events relative to LW face after Luo et al. [14] (intentionally rotated)

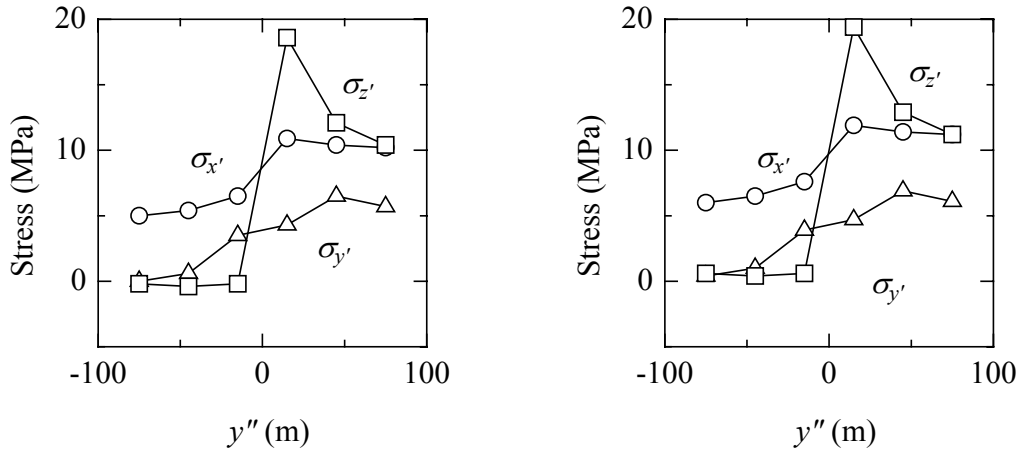

(a) 15 m above coal seam (b) 15 m below coal seam

Fig. 6 Stress distribution at 1020 m face advance

rock elements above and below the mined area are due to the maximum principal stress in nearly EW direction and the reduced nearly vertical minimum principal stress. The distribution of the broken elements in the plan view is gradually biased to the tailgate. This can be clearly seen when the face reaches 390 m from the setup entry. This biased distribution is mainly due to broken elements with relatively small maximum shear seismic moments since the biased distribution is not observed in Fig. 8 which shows broken elements with relatively large maximum shear seismic moments. A biased distribution similar to the simulated results can be seen in the observed microseismic events (Fig. 5a). However, relatively strong events distributed rather evenly.

The maximum height of broken elements in the roof increases gradually as the face advances up to 500 m and is kept almost constant (Fig. 9). Cluster of broken elements just as forming a plane often appear in the roof as the face advances up to 240 m (Figs. 7b and 7c). This might correspond to the observed main fall of the roof when the shape of the mined area became almost square. No cluster was observed in the following face advance because the yield zone ahead of the face is high enough and there are no unbroken elements left behind the face.

EFFECTS OF STRENGTH

Strengths in Case A-0.5 are as low as a half of those in Case A-1. The behavior of the broken elements' distribution (Fig. 10a) is similar to the observation. However, the height of the yield zone is larger than the observation. Strengths, which are five times larger than Case A-1, were used in Case A-5. The size of the yield zone is significantly smaller than the observation (Fig. 10b). The biased distribution is not observed.

EFFECTS OF HORIZONTAL STRESS

Results of case B-1, where both the horizontal components of initial stress are 0.48 times the vertical component, are shown in Fig. 10c. There is no similarity between behavior of the simulated broken elements and the observed biased distribution of microseismic events. This is because the rock elements, which have to be kept intact in order to exhibit the biased distribution, had already been broken before the mining of LW4.

Horizontal stresses in EW and NS directions are both 1.2 times the vertical stress in Case C-1. All broken elements were located behind the face (Fig. 10d). Compressive failure of rock mass, which is due to horizontal maximum principal stress and vertical minimum principal stress, dominates. This is because the larger horizontal stress in the retreat direction prevents failure of rock mass ahead of the face. This feature is totally different from the observation. A few tensile failure of rock mass were also observed.

Table 2 Initial stress variation

X	A	B	C
E_{rock} / E_{coal}	2		
Poisson' ratio	0.2		
Vertical stress	Product of specific gravity and depth		
Specific gravity	27 kN/m^3		
σ_x (EW)	1.20 σ_V	0.48 σ_V	1.20 σ_V
σ_y (NS)	0.48 σ_V	0.48 σ_V	1.20 σ_V
Working height	4.5 m		

Table 3 Strength variation

n	0.5		1		5	
	Rock	Coal	Rock	Coal	Rock	Coal
Tensile strength (MPa)	0.25	0.125	0.5	0.25	2.5	1.25
Residual tensile strength (MPa)	0.225	0.1125	0.45	0.225	2.25	1.125
Uniaxial compressive strength (MPa)	0.5	0.25	1	0.5	5	2.5
Residual compressive strength (MPa)	0.45	0.225	0.9	0.45	4.5	2.25
Angle of internal friction (degree)	30	30	30	30	30	30

EXISTENCE OF COAL ROOF

Numerical simulation was carried out for Case A-1'. This is based on Case A-1, however, strength for coal seam was assigned to the immediate roof strata. Stress distribution is not correct since the elastic constants for the immediate roof is still for rock mass.

The intensity of microseismic events in the immediate coal roof were much weaker than that in the main roof in the microseismic observation. This was not observed in the simulated results. This discrepancy might suggest that this numerical model is still not precise enough. It can also be pointed out that the calculated fracturing intensity for microseismic events from the coal roof in the observation would be less than the reality since elastic wave from a severely fractured coal roof would be much more attenuated than that from rock mass.

EFFECTS OF PANEL LAYOUT

Numerical simulations were finally carried out for three imaginary panel layouts (Fig. 11). Case A-1-a is for a single mining panel without any other mined areas. Setup entry is excavated parallel to that of LW3 in Case A-1-b. The position of the setup entry is 210 m ahead of that of LW3 in Case A-1-c.

Case A-1-a

Normal stress distribution is shown in Fig. 12a. Stress concentration on the edges of mined area is significantly less than Case A-1. The biased distribution of the stress concentration area cannot be seen. Results of numerical simulation on microseismicity are shown in Fig. 13a. The size of the yield zone is smaller than Case A-1 and the biased distribution of broken elements cannot be seen. However, the height of the yield zone and its growth behavior were almost the same as Case A-1 (Fig. 9).

Case A-1-b

Both the normal stress distribution and the distribution of broken elements are almost the same as case A-1, except that the biased distribution of stress concentration area and that of broken elements can be observed earlier than Case A-1. Height of the yield zone is almost the same as case A-1.

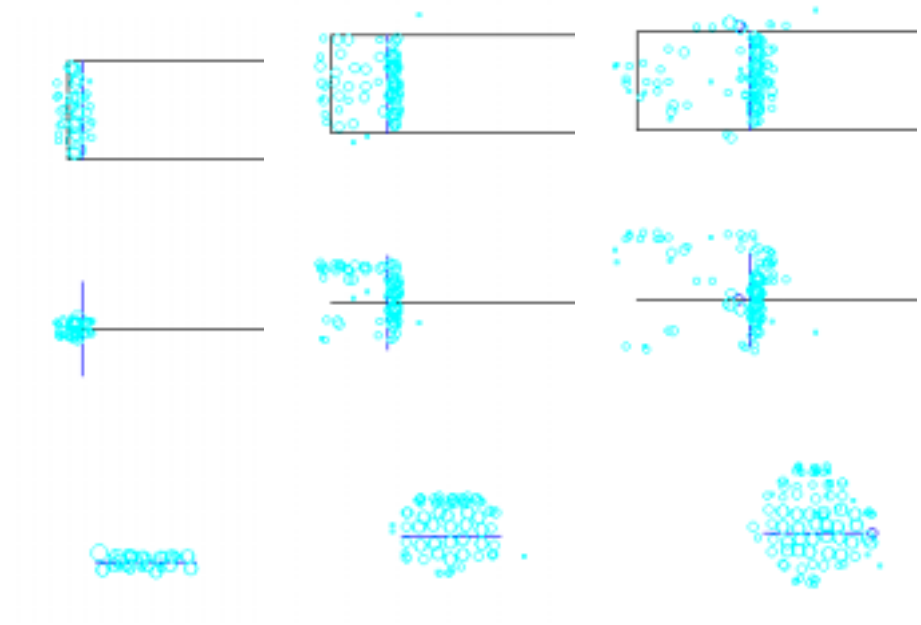

(a) 30 m (b) 120 m (c) 240 m

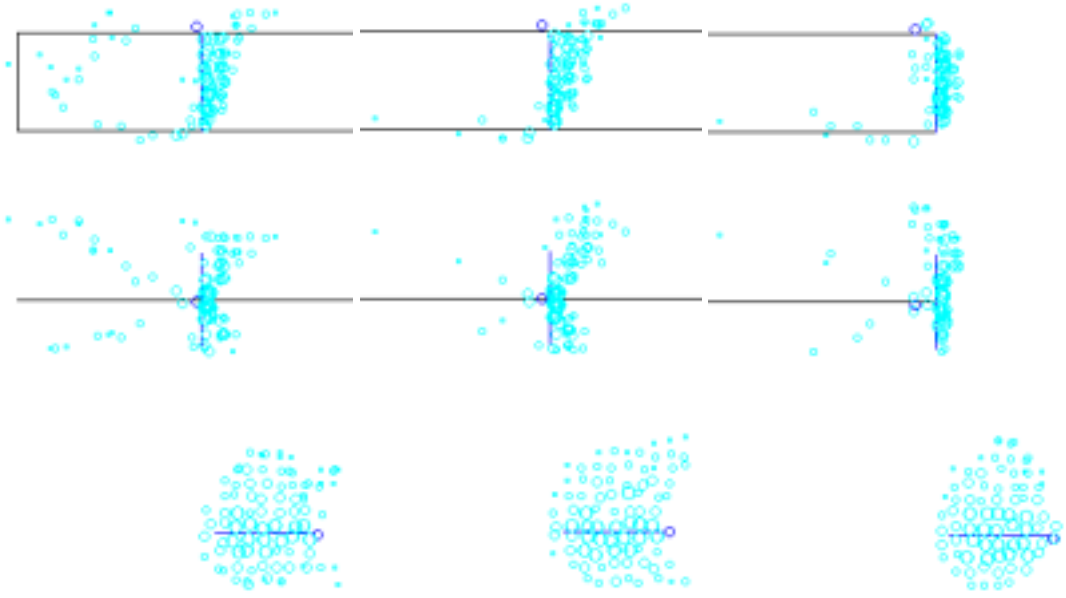

(d) 390 m (e) 1170 m (f) 2280 m

Fig. 7 Distribution of broken elements in Case A-1. There are three rows of drawings - the top ones are plan view (x'-y'), the middle ones are longitudinal cross-section (y'-z', along mining direction) view, and the bottom ones are end view (x'-z'). The radiuses of the circles are proportional to the logarithm of maximum shear seismic moment. Locations of the circles are displaced randomly up to h / 2 in order to avoid overlapping. Gray and black circles denote compressive failure of rock mass and coal seam, respectively. Tailgate is right side and maingate is left side in the x'-z' section.

Fig. 8 Broken elements having maximum shear seismic moments which are greater than 5 GN·m (Case A-1, 1170 m). The top ones are plan view (x'-y'), the middle ones are longitudinal cross-section (y'-z', along mining direction) view, and the bottom ones are end view (x'-z').

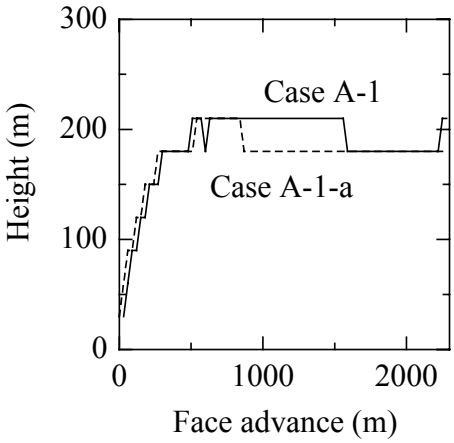

Fig. 9 Maximum height of broken elements

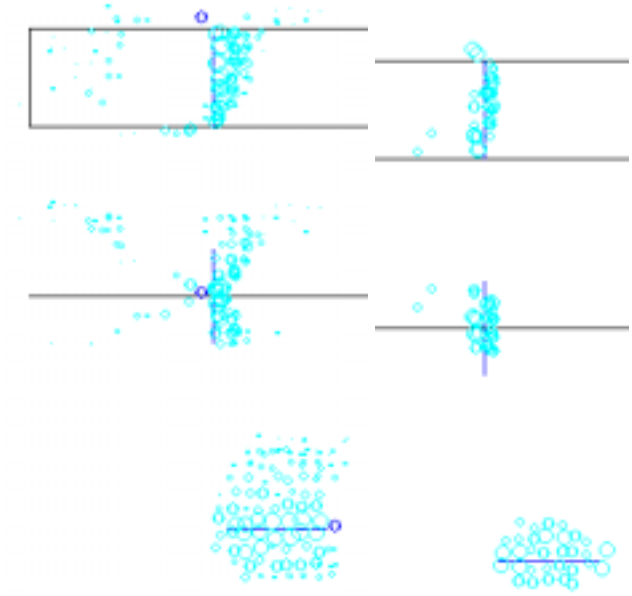

(a) Case A-0.5 (weak case) (b) Case A-5 (strong case)

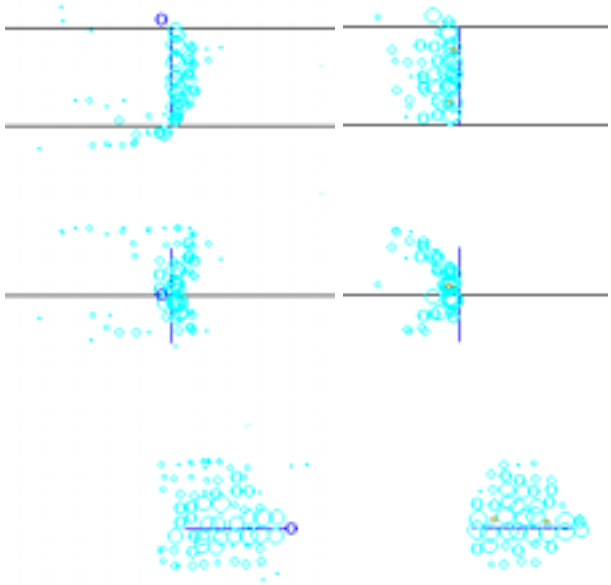

(c) Case B-1 (small stress case) (d) Case C-1 (large stress case)

Fig. 10 Broken elements for various strengths or under various initial stresses. The top ones are plan view (x'-y'), the middle ones are longitudinal cross-section (y'-z', along mining direction) view, and the bottom ones are end view (x'-z').

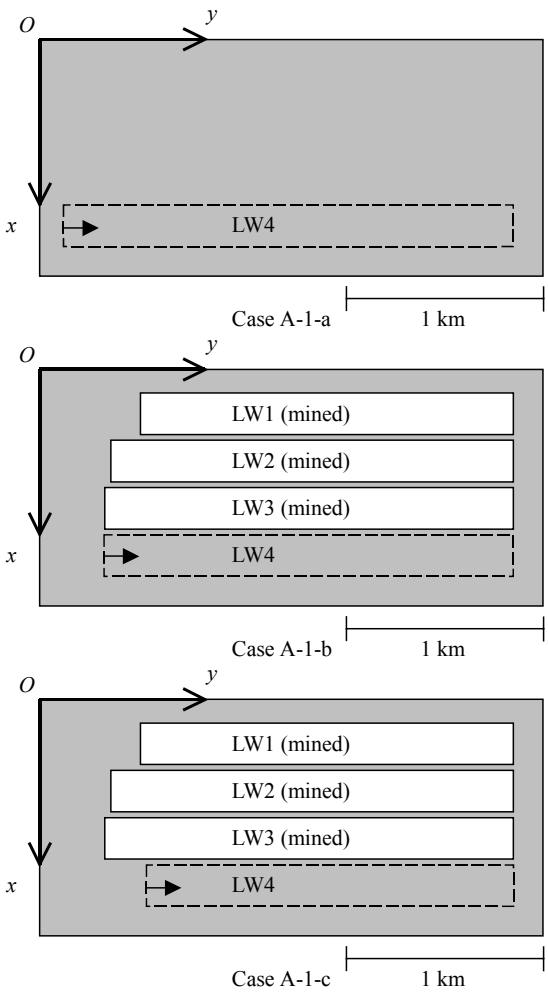

Fig. 11 Three imaginary panel layouts.

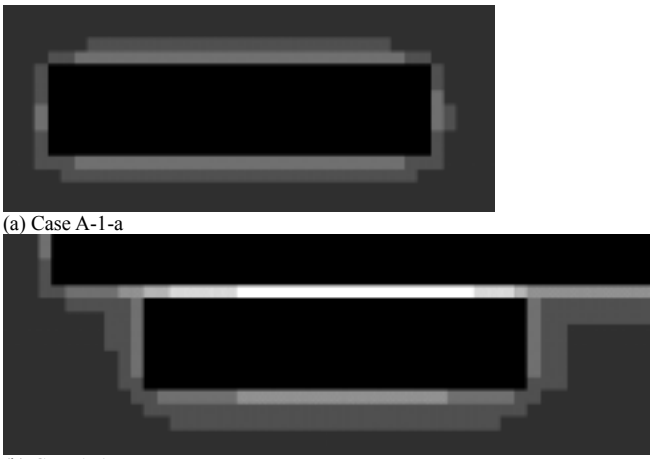

(a) Case A-1-a

(b) Case A-1-c

Fig. 12 Normal stress distribution for two imaginary panel layouts

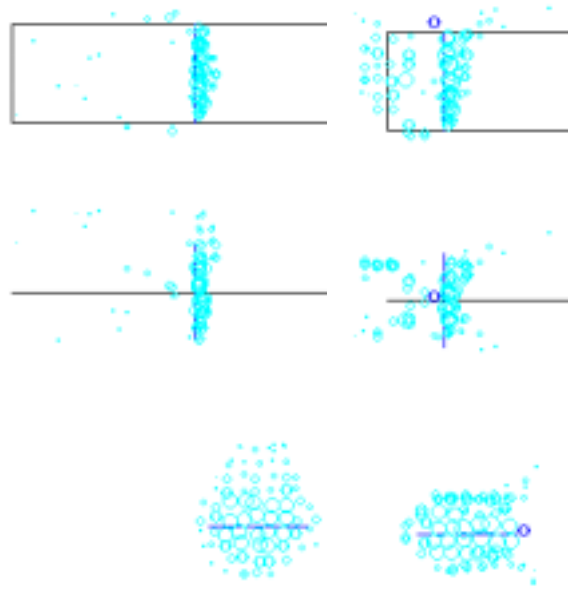

(a) Case A-1-a (b) Case A-1-c

Fig. 13 Distribution of broken elements for two imaginary panel layouts. The top ones are plan view (x'-y'), the middle ones are longitudinal cross-section (y'-z', along mining direction) view, and the bottom ones are end view (x'-z').

Case A-1-c

Normal stress distribution is shown in Fig. 12b. The biased stress concentration area can be seen behind the setup entry as well as ahead of the face. The stress distribution pattern is almost the same as case A-1 except for the biased distribution behind the setup entry. The results of numerical simulation are shown in Fig. 13b. Broken elements concentrate on the setup entry as well as on the coal face. The biased distribution is observed even earlier than Case A-1-b. Height of the yield zone is almost the same as Case A-1.

CONCLUSIONS

Numerical simulation for microseismicity due to mining at one of the collieries in Australia was carried out and the results were compared to the observed microseismicity.

3-D Stress analysis showed stress concentration on the edges of the mined areas and on the coal pillars. The stress concentration ahead of the coal face was biased to the tailgate. This is similar to the observed distribution of microseismic events.

Distribution of stress components around coal face was investigated. Compressive failure due to nearly vertical maximum principal stress and nearly horizontal minimum principal stress in the retreat direction ahead of the face were expected. It was expected that tensile failure due to nearly vertical minimum principal stress might occur above the mined area. Compressive failure due to nearly horizontal maximum principal stress in EW direction and nearly vertical minimum principal stress above and below the mined area was also expected.

Numerical simulation on microseismicity due to the mining of LW4 was carried out with a standard initial stress and strength data set. Broken elements were mainly distributed 0 to 100 m ahead of the face with more such elements in the roof than in floor. Distribution of the broken elements with relatively small maximum shear seismic moments in plan view was biased to the tailgate. On the other hand, broken elements with relatively large maximum shear seismic moments were distributed evenly. This behavior is similar to the observation that weak microseismic events showed a biased distribution while the strong ones were distributed evenly. The height of the yield zone was initially 30 m and increased gradually as

the face advances up to 500 m. It was thereafter kept almost constant. Cluster of broken elements just as forming a plane often appeared in the roof as the face advanced up to 240 m. This might correspond to the observed main fall of the roof when the shape of the mined area became almost square.

Effects of strength on the simulated results were investigated. It was confirmed that the larger the strength data, the smaller the yield zone. Similar features with microseismic observation were obtained for the results with smaller strength data although there was no similarity between the simulated results with larger strength data and the microseismic observation. The selected best strength data values were very small compared to the laboratory values. This might suggest that the observed microseismicity reflects slip and opening of planes of weakness.

Effects of initial horizontal stress were investigated. It was clarified that the biased distribution of broken elements was not observed when smaller horizontal stresses were assumed. Broken elements appeared behind the face when larger horizontal stresses were used. The results suggest that the initial horizontal stress affects significantly on failure around longwall mining panels.

Effects of panel layout were investigated by carrying out simulation for three imaginary panel layouts. It was realized that stress concentration on the edges of mined area was significantly small when there was no gobs but LW4 itself. Neither the biased distribution of the stress concentration nor the biased distribution of broken elements was seen. No significant difference in the height of the yield zone and its growth behavior from the standard case were observed. In the case where the setup entry was set parallel to that of LW3, no significant difference from the standard case was observed in the normal stress distribution or distribution of broken elements except that the biased distributions were observed earlier than the standard case. The height of the yield zone did not seem to be affected by the change in panel layout. In the case where the setup entry position was 210 m ahead of that of LW3, a biased stress concentration area behind the setup entry was observed. Broken elements concentration on the setup entry was observed in the initial stage of mining. The biased distribution of broken elements ahead of the face was observed even earlier than the previous case. The behavior of the yield zone height was similar to the standard case.

The above results are basically reasonable comparing to the microseismic observation. It is considered that they are offering valuable clues to understand deformation and failure around longwall mining panels. Some of the results can only be obtained by using 3-D analysis. This suggests the importance of a 3-D numerical stress analysis for strata control in longwall coal mining. However, the simulation method should be further sophisticated to give even better results. For instance, such inhomogeneity as multi strata structure, dykes, etc. cannot be simulated at present.

REFERENCES

1. Cook, N. G. W., Hoek, E., Pretorius, J. P. G., Ortlepp, W. D. and Salamon, M. D. G. (1966), Rock Mechanics Applied to the Study of Rockburst. J. South Afr. Inst. Min. Metall, Vol. 66, No. 10, pp. 435-528
2. Sugawara, K., Obara, Y. and Kaneko, K. (1986 in Japanese), Prediction of Microseismicity Associated with Longwall Coal Mining, Proc. MMIJ Spring Meeting, pp. 283-284
3. McGarr, A. and Wiebols, G. A. (1977), Influence of Mine Geometry and Closure Volume on Seismicity in a Deep-Level Mine, Int. J. Rock Mech. Min. Sci. & Geomech. Abstr, Vol. 14, pp. 139-145
4. Ryder, J. A. (1988), Excess Shear Stress in the Assessment of Geologically Hazardous Situations, J. S. Afr. Inst. Min. Metall., Vol. 88, No. 1, pp. 27-39
5. Spottiswoode, S. M. (1988), Total Seismicity, and the Application of ESS Analysis to Mine Layouts. J. S. Afr. Inst. Min. Metall, Vol. 88, No. 4, pp. 109-116
6. Spottiswoode, S. M. (1988), Volume Excess Shear Stress and Cumulative Seismic Moments. Pre-printed Papers, 2nd. Intl. Symp. Rockbursts and Seismicity in Mines, Minneapolis, Minnesota, pp. 1-12
7. Fujii, Y. and Ishijima, Y. (1988 in Japanese), Microseismicity Induced by Deep Coal Mining and Its Numerical Simulation, J. MMIJ, Vol. 104, No. 1204, pp. 345-351
8. Fujii, Y. and Ishijima, Y. (1991), Numerical Simulation on Microseismicity Induced by Deep Longwall Coal Mining, Min. Sci. & Tech., Vol. 12, No. 3, pp. 265-285
9. Fujii, Y., Ishijima, Y. and Deguchi, G. (1997), Prediction of Coal Face Rockbursts and Microseismicity in Deep Longwall Coal Mining, Int. J. Rock Mech. Min. Sci. & Geomech. Abstr., Vol. 34, No. 1, pp. 85-96
10. Crouch, S.L. and Fairhurst, C. (1973): The Mechanics of Coal Mine Bumps and the Interaction between Coal Pillars, Mine Roof and Floor, U. S. B. M. Contract Report, H0101778
11. Aki, K. and Richards, P. G. (1980), Quantitative Seismology, Theory and Methods. 1, W. H. Freeman and Company, San Francisco
12. Miyamoto, H. (1967 in Japanese), Elastic Theory in Three Dimension, Shokabo, Tokyo
13. Sato, K. and Kinoshita, S. (1976 in Japanese), Griffith Locus in Compressive Deformation, J. MMIJ., Vol. 92, pp. 409-414
14. Luo X., Ross J., King A. (2000), Microseismic Monitoring at Dartbrook Mine for Underground Gas Emission Control, CSIRO Report No. 675.

APPENDIX

Evaluation of stress components in coal seam apart from coal face by several times the working height

Assume a homogeneous, isotropic elastic medium and that Young's modulus, rigidity, Poisson's ratio are represented by E_C, G_C, ν_C for coal seam and E_R, G_R, ν_R for rock mass. The normal of the coal seam is taken as z-axis. Traction of coal seam τ_{xz}, τ_{yz}, σ_z and stress component σ_{xR}, σ_{yR}, τ_{xyR} on the surface of rock which contacts to coal seam are given by DDM. Since a coal seam element is of a tabular shape, strain components in rock mass ε_{xR}, ε_{yR}, γ_{xyR} are equivalent to those in coal seam ε_{xC}, ε_{yC}, γ_{xyC} assuming that there is no slip on the boundary between coal and rock. By using this relationship, stress components in coal seam σ_{xC}, σ_{yC}, γ_{yC} can be represented as follows.

$$\sigma_{xC} = (\lambda_C + 2\mu_C)\varepsilon_{xR} + \lambda_C\varepsilon_{yR} + \lambda_C\varepsilon_{zC} \quad \text{(A1)}$$

$$\sigma_{yC} = (\lambda_C + 2\mu_C)\varepsilon_{yR} + \lambda_C\varepsilon_{xR} + \lambda_C\varepsilon_{zC} \quad \text{(A2)}$$

$$\tau_{xyC} = \mu_C\gamma_{xyR} \quad \text{(A3)}$$

$$\varepsilon_{zC} = \frac{\sigma_z}{E_C} - \nu_C\frac{\sigma_{xC} + \sigma_{yC}}{E_C} \quad \text{(A4)}$$

Where λ_C, μ_C are Lame's constants for coal seam, ε_{zC} is the vertical strain component in coal seam.

Hooke's law for rock mass can be represented as follows.

$$\varepsilon_{xR} = \frac{\sigma_{xR}}{E_R} - \nu_R\frac{\sigma_{yR} + \sigma_z}{E_R} \quad \text{(A5)}$$

$$\varepsilon_{yR} = \frac{\sigma_{yR}}{E_R} - \nu_R\frac{\sigma_{xR} + \sigma_z}{E_R} \quad \text{(A6)}$$

$$\gamma_{xyR} = \frac{\tau_{xyR}}{G} \quad \text{(A7)}$$

The following equations on stress components in coal seam are obtained by substituting Eqs.(A4) to (A6) into Eqs.(A1) and (A2), Eq.(A7) into Eq.(A3) and by assuming $\nu_C = \nu_R = \nu$.

$$\sigma_{xC} = \frac{E_C}{E_R}\{\sigma_{xR} - \nu(1-\nu)\sigma_z\} + \nu(1-\nu)\sigma_z \quad \text{(A8)}$$

$$\sigma_{yC} = \frac{E_C}{E_R}\{\sigma_{yR} - \nu(1-\nu)\sigma_z\} + \nu(1-\nu)\sigma_z \quad \text{(A9)}$$

$$\tau_{xyC} = \frac{E_C}{E_R}\tau_{xyR} \quad \text{(A10)}$$